

# Schrödinger's Smoke

Albert Chern  
Caltech

Felix Knöppel  
TU Berlin

Ulrich Pinkall  
TU Berlin

Peter Schröder  
Caltech

Steffen Weißmann  
Google Inc.

## Abstract

We describe a new approach for the purely Eulerian simulation of incompressible fluids. In it, the fluid state is represented by a  $\mathbb{C}^2$ -valued wave function evolving under the Schrödinger equation subject to incompressibility constraints. The underlying dynamical system is Hamiltonian and governed by the kinetic energy of the fluid together with an energy of Landau-Lifshitz type. The latter ensures that dynamics due to thin vortical structures, all important for visual simulation, are faithfully reproduced. This enables robust simulation of intricate phenomena such as vortical wakes and interacting vortex filaments, even on modestly sized grids. Our implementation uses a simple splitting method for time integration, employing the FFT for Schrödinger evolution as well as constraint projection. Using a standard penalty method we also allow arbitrary obstacles. The resulting algorithm is simple, unconditionally stable, and efficient. In particular it does not require any Lagrangian techniques for advection or to counteract the loss of vorticity. We demonstrate its use in a variety of scenarios, compare it with experiments, and evaluate it against benchmark tests. A full implementation is included in the ancillary materials.

**Keywords:** discrete differential geometry, fluid simulation, Schrödinger operator

**Concepts:** •Mathematics of computing → Partial differential equations; •Computing methodologies → Physical simulation; •Applied computing → Physics;

## 1 Introduction

We introduce *incompressible Schrödinger flow* (ISF), a new method to simulate incompressible fluids (Fig. 1, middle). Instead of describing the fluid evolution in terms of the velocity or vorticity field, ISF evolves a two-component wave function  $\psi = (\psi_1, \psi_2)^\top: M \rightarrow \mathbb{C}^2$ , which encodes the fluid state on a 3D domain  $M$ . The classical fluid density  $\rho$  and fluid velocity  $v = (v_1, v_2, v_3)^\top$  are extracted from  $\psi$  as

$$\rho = |\psi|^2 = \langle \psi, \psi \rangle_{\mathbb{R}} \quad \text{and} \quad \rho v_\alpha = \hbar \langle \frac{\partial \psi}{\partial x_\alpha}, i\psi \rangle_{\mathbb{R}} \quad \alpha = 1, 2, 3$$

where  $\langle \phi, \psi \rangle_{\mathbb{R}} = \text{Re}(\langle \phi, \psi \rangle_{\mathbb{C}}) = \text{Re}(\bar{\phi}_1 \psi_1 + \bar{\phi}_2 \psi_2)$ . The time evolution of these wave functions is governed by the Schrödinger equation

$$i\hbar \dot{\psi} = -\frac{\hbar^2}{2} \Delta \psi + p \psi \quad \frac{\partial \psi}{\partial N} \Big|_{\partial M} = 0 \quad (1)$$

Permission to make digital or hard copies of all or part of this work for personal or classroom use is granted without fee provided that copies are not made or distributed for profit or commercial advantage and that copies bear this notice and the full citation on the first page. Copyrights for components of this work owned by others than ACM must be honored. Abstracting with credit is permitted. To copy otherwise, or republish, to post on servers or to redistribute to lists, requires prior specific permission and/or a fee. Request permissions from permissions@acm.org. © 2016 ACM.

SIGGRAPH '16 Technical Paper, July 24-28, 2016, Anaheim, CA  
ISBN: 978-1-4503-4279-7/16/07  
DOI: <http://dx.doi.org/10.1145/2897824.2925868>

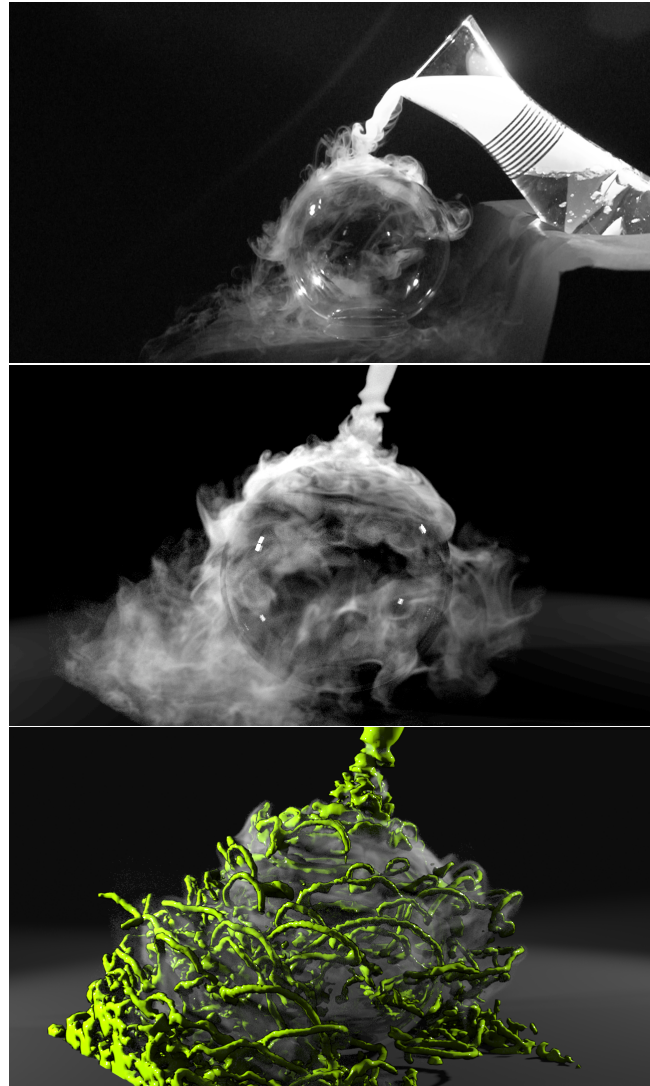


Figure 1: Comparing experiment (dry ice vapor, top) with ISF simulation (middle), followed by a visualization of the underlying wave function  $\psi$ . Vorticity is concentrated within the green region.

subject to the constraints

$$\langle \Delta \psi, i\psi \rangle_{\mathbb{R}} = 0 \quad \text{and} \quad |\psi|^2 = 1, \quad (2)$$

which correspond to  $\text{div}(v) = 0$  and  $\rho = 1$  in the classical variables (Sec. 4.1). The scalar potential  $p: M \rightarrow \mathbb{R}$  in Eq. (1) is the Lagrange multiplier for the divergence constraint (App. A), and we will refer to it as *pressure* in analogy to the Euler equation. The *reduced Planck constant*  $\hbar$  of quantum Physics becomes the *only parameter* for our fluid and controls the quantization of vorticity. For a large range of initial conditions ISF tends to concentrate vorticity in filaments of strength  $2\pi\hbar$  (Fig. 1, bottom).

We call Eqs. (1) and (2) the *incompressible Schrödinger equations* and the corresponding flow the incompressible Schrödinger flow.

ISF is computationally very attractive. Using a splitting method for time integration, each step requires only linear Schrödinger evolution, followed by normalization and pressure projection, *i.e.*, solution of a Poisson problem (Alg. 1). All advection happens within the Schrödinger evolution, no separate advection step is needed. The resulting algorithm is unconditionally stable, straightforward to implement, and efficient. Obstacles are also easily incorporated (Alg. 4).

ISF is a Hamiltonian flow with respect to the energy

$$H_{\text{ISF}}(\psi) = \frac{\hbar^2}{2} \|d\psi\|^2 = \frac{1}{2} \|v\|^2 + \frac{\hbar^2}{4} H_s(\psi) \quad (3)$$

(Thm. 2, Sec. 4.4) with  $\|\cdot\|$  denoting the  $L^2$  norm. The kinetic energy alone (first summand) would give the Euler equations for ideal, *i.e.*, inviscid and incompressible, fluids. In ISF these equations are modified by the presence of the term  $H_s$  (Secs. 4.2–4.5). For flows dominated by vortex filaments it can be interpreted geometrically as approximating the  $4\pi$  multiple of the length of all vortex filaments in the fluid (Sec. 4.5).

This modification has significant consequences for incompressible fluid simulation on grids. Standard methods using a direct velocity or vorticity representation typically struggle with maintaining coherent vortical structures and their dynamics over time (Sec. 1.2). These structures are usually concentrated along curves and often persist over significant periods of time, while their dynamics are critical for the visual appearance of flows (Fig. 1, cmp. top and middle). ISF captures their energy in  $H_s$ , preserving vortical structures and their dynamics over a wide range of scales on modest resolution grids.

**Note** To simplify the derivations we will use Exterior Calculus [Abraham et al. 2001, Ch. 6] in the remainder of the paper, working with the velocity 1-form  $\eta = v^\flat = \hbar \langle d\psi, i\psi \rangle_{\mathbb{R}}$  instead of  $v$  and correspondingly  $*d*\eta = 0$  instead of  $\text{div}(v) = 0$ .

Notation	Meaning
$\psi = (\psi_1, \psi_2)^\top : M \rightarrow \mathbb{C}^2$	wave function
$\dot{\psi} = \frac{\partial \psi}{\partial t}$	time derivative
$d\psi$	differential of $\psi$
$\langle \phi, \psi \rangle_{\mathbb{C}} = \bar{\phi}_1 \psi_1 + \bar{\phi}_2 \psi_2$	Hermitian form on $\mathbb{C}^2$
$\langle \phi, \psi \rangle_{\mathbb{R}} = \text{Re}(\langle \phi, \psi \rangle_{\mathbb{C}})$	Euclidean product on $\mathbb{C}^2$
$ \psi ^2 = \langle \psi, \psi \rangle_{\mathbb{R}}$	pointwise squared norm
$\langle u, v \rangle$	Euclidean product on $\mathbb{R}^3$
$2\pi\hbar$	vortex filament strength
$\eta = v^\flat = \hbar \langle d\psi, i\psi \rangle_{\mathbb{R}}$	velocity 1-form
$\omega = d\eta$	vorticity 2-form
$\xi = *d*\eta$	divergence
$\mathcal{L}_v \psi = (v \cdot \nabla) \psi$	Lie derivative of $\psi$
$\mathcal{L}_v \eta = ((v \cdot \nabla) v + \frac{1}{2} \nabla  v ^2)^\flat$	Lie derivative of $\eta$

Table 1: Notations used.

## 1.1 Physics Foundations

In the context of fluids the Schrödinger equation typically only appears in the study of fluids at very low temperatures and very small scales, so called *superfluids*. Despite this, superfluid dynamics are of great interest for computer graphics applications because of the remarkable similarities between vortex dynamics

in ordinary and superfluids, both at the experimental and theoretical levels [Schwarz 1985] (see also the more recent [Stagg et al. 2014] and references therein).

In most situations of practical import the dynamics of ordinary fluids are dominated by thin vortex filaments [Saffman 1992]. Because of their thinness these are inherently difficult to resolve at feasible grid resolutions with traditional representations (*ibid*, p. 201). In superfluids, using wave functions to describe the state of the system, such filaments are a topological feature and thus far more persistent and computationally resolvable even at relatively modest resolutions.

Early on in the history of the study of superfluids it was recognized that they carry quantized vorticity in atomic scale filaments [Onsager 1949; Feynman 1955]. These were later experimentally verified [Hall and Vinen 1956] and even photographed [Packard and Sanders 1969]. In our approach the strength of the filaments is  $2\pi\hbar$ , which we can take as a *quantization parameter* of our simulations, setting the strength of vortex filaments and with it the level of detail present in the flow.

A mathematical model for the observed physics of superfluids was developed by Gross [1961] and Pitaevskii [1961] (and earlier Ginzburg and Pitaevskii [1958]). This model is now known as the *Gross-Pitaevskii* (GP) equation, or simply the *non-linear Schrödinger* (NLS) equation

$$i\hbar\dot{\varphi} = -\frac{\hbar^2}{2} \Delta \varphi + \frac{1}{a^2} (|\varphi|^2 - 1) \varphi,$$

for  $\varphi : M \rightarrow \mathbb{C}$  and a parameter  $a > 0$  which for us corresponds to the core radius of vortex filaments.

The non-linear (cubic) term acts as a potential opposing the deviation of the density  $\rho = |\varphi|^2$  from 1. Indeed, in simulations using the GP equation the density is near 1 in most of the domain, save for the zero set of  $\varphi$  in whose vicinity the density smoothly decreases to zero [Stagg et al. 2014]. Taking the limit  $a \rightarrow 0$  one expects the non-linear term to converge to the incompressible limit and hence the GP equation to recover the Euler equations for  $\eta$ . In 2D this has been rigorously established [Lin and Xin 1999; Jerrard and Spirn 2015].

As a practical matter, choosing a small  $a$  in the cubic term leads to very stiff numerical problems. Since we are only interested in the incompressible setting, we can replace the cubic non-linearity with the incompressibility constraints. For single component wave functions the uniform density constraint  $|\varphi|^2 = 1$  yields singular  $\varphi$  and allows for irrotational velocity fields only. Using instead a two-component wave function  $\psi : M \rightarrow \mathbb{C}^2$  leaves  $\psi$  smooth under the constraint  $|\psi|^2 = 1$ . Additionally it allows for smoothly varying vorticity [Schönberg 1954; Sorokin 2001].

The interpretation of the Schrödinger equation in terms of fluids was first pursued by Madelung [1926; 1927] in an effort to elucidate the then new quantum mechanics. He showed that the Schrödinger equation for single component wave functions is equivalent to the quantum Euler equations. What became known as the Madelung transform was later applied to  $\mathbb{C}^n$ -valued wave functions by Schoenberg [1954]. In particular he introduced the form of  $\eta$  we use. Sorokin [2001] gave the  $\mathbb{C}^2$  version of the Madelung transform including explicit expressions for the non-linear potentials which distinguish it from the classical Euler fluid.

Two threads from Physics have influenced our work. On one hand the hydrodynamical interpretation of Quantum Physics and on the other the GP equation for the modeling of superfluids. Since we are interested in incompressibility we replace the numerically

stiff cubic term in the GP equation with pressure projection. At the same time our fluid inherits the robust representation of vortex filaments from superfluids.

## 1.2 Vorticity in Computer Graphics

The importance of vorticity for visual simulation has long been recognized in computer graphics, as has the difficulty to capture its dynamics correctly with numerical methods.

The success of Jos Stam’s “Stable Fluids” [1999] method, using semi-Lagrangian advection and pressure projection on a regular grid, quickly led to work addressing its excessive numerical diffusion [Fedkiw et al. 2001] using vorticity confinement [Steinhoff and Underhill 1994]. Lost detail has also been compensated by wavelet turbulence [Kim et al. 2008] or curl-noise [Bridson et al. 2007]. Unfortunately, these techniques are difficult to control and easily lead to objectionable visual artifacts.

Alternatively one can represent vorticity through Lagrangian vortex particles, a technique from the CFD community [Rosenhead 1931; Leonard 1980; Cottet and Koumoutsakos 2000] to avoid many of these issues [Park and Kim 2005]. Since vorticity arises at boundary layers as sheets and then quickly rolls up into filaments, purely Lagrangian methods based on filaments [Angelidis and Neyret 2005; Weißmann and Pinkall 2010] and sheets [Stock et al. 2008; Brochu et al. 2012] have also been developed.

Using vorticity as a primary variable also improves mesh based Eulerian simulations [Elcott et al. 2007], motivating [Zhang et al. 2015] to modify existing velocity based Eulerian solvers to perform as if using vorticity as their primary variable.

Many recent approaches are of a hybrid nature, integrating Lagrangian elements into grid based approaches [Selle et al. 2005; Kim et al. 2009; Pfaff et al. 2012] or enhancing purely Lagrangian methods with grids [Koumoutsakos et al. 2008].

Overall we see that proper resolution of vorticity is essential to the visual appearance of flows and simultaneously difficult to achieve. Grid based approaches battle loss of vorticity with various devices, while purely Lagrangian approaches have their own host of problems ranging from inadequate control of sample density (particles), to complex reconnection handling (filaments), and the need for sophisticated multipole solvers, etc..

Our new method is grid based and purely Eulerian. Still we are able to simulate vortex driven dynamics, with grids of modest sizes, at a quality level comparable to purely Lagrangian methods.

## 2 The Algorithm

All our simulations are performed on a 3D lattice with vertex set  $\mathcal{V} = \{0, \dots, \mathcal{N}_x - 1\} \times \{0, \dots, \mathcal{N}_y - 1\} \times \{0, \dots, \mathcal{N}_z - 1\}$ . For a periodic domain, indices are taken modulo their respective dimension. Vertices,  $v \in \mathcal{V}$ , need to store samples of the wave function  $\psi_v \in \mathbb{C}^2$ , the real-valued pressure  $q_v \in \mathbb{R}$ , and the real-valued divergence  $\xi_v \in \mathbb{R}$ . The discrete velocity 1-form is defined on directed edges  $vw \in \mathcal{E}$

$$\eta_{vw} := \hbar \arg(\psi_v, \psi_w)_c \quad (4)$$

with  $\eta_{vw} = -\eta_{wv}$  (App. D) and stored in staggered grid fashion at the vertices (Fig. 2).

The discrete divergence,  $\xi = *d*\eta$ , is the usual signed sum over incident edges, weighted by the quotient of dual facet area  $A_{vw}$  to

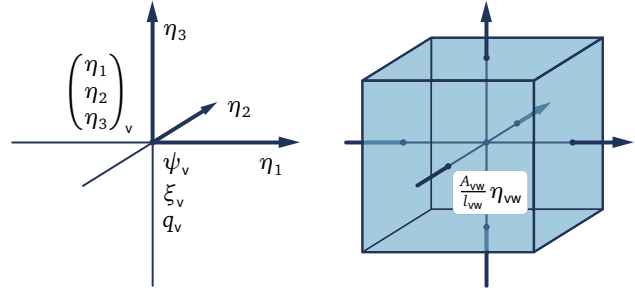


Figure 2: In all, 9 reals are stored at vertices:  $\psi_v$ ,  $\xi_v$ ,  $q_v$ , and the three circulations  $(\eta_1, \eta_2, \eta_3)^\top$  associated with the edges emanating in the positive coordinate directions. The divergence  $\xi_v$  is the normalized sum of the face fluxes  $\frac{A_{vw}}{l_{vw}} \eta_{vw}$  on the enclosing cube.

edge length  $l_{vw}$  and normalized by dual cell volume  $V_v$  (Fig. 2)

$$\xi_v = (*d*\eta)_v = \frac{1}{V_v} \sum_{vw \in \mathcal{E}} \frac{A_{vw}}{l_{vw}} \eta_{vw}, \quad (5)$$

following standard Discrete Exterior Calculus (DEC) conventions [Desbrun et al. 2008; Crane et al. 2013].

**Overall time integration** uses operator splitting, performing integration of the Laplace term, normalization, and pressure projection in order. Later we include obstacles and buoyancy resp. gravity forces.

Time integration requires an initial  $\psi^{(0)}$ , a time step size  $dt > 0$ , and a quantization strength  $\hbar > 0$ . Appropriate values will be illustrated with the aid of example simulations (Sec. 3 and Tbl. 2).

---

### Algorithm 1 Basic ISF

**Input:**  $\psi^{(0)}, dt, \hbar$  Initial state and parameters  
 1: **for**  $j \leftarrow 0, 1, 2, \dots$  **do**  
 2:    $\psi^{\text{tmp}} \leftarrow \text{SCHRÖDINGER}(\psi^{(j)}, dt, \hbar)$   
 3:    $\psi^{\text{tmp}} \leftarrow \psi^{\text{tmp}} / |\psi^{\text{tmp}}|$  Normalization  
 4:    $\psi^{(j+1)} \leftarrow \text{PRESSUREPROJECT}(\psi^{\text{tmp}})$   
 5: **end for**

---

**Schrödinger integration** diagonalizes in the Fourier domain, leading us to use the FFT (on periodic domains). For walls  $\partial M \neq \emptyset$  Neumann boundary conditions are achieved with the discrete cosine transform (DCT). Here  $\lambda_v$  are the eigenvalues of the continuous 3D Laplace operator (Eq. (18), App. E).

---

### Algorithm 2 Time integration of Schrödinger equation

1: **function** SCHRÖDINGER( $\psi, dt, \hbar$ )  
 2:    $\hat{\psi} \leftarrow \text{FFT3D}(\psi)$   
 3:    $\hat{\psi} \leftarrow e^{i\lambda dt \frac{\hbar}{2}} \hat{\psi}$   
 4:   **return**  $\text{INVFFT3D}(\hat{\psi})$   
 5: **end function**

---

**Pressure projection** Eq. (10) uses the scaled ( $\hbar^{-1}$ ) discrete divergence as the right hand side of a Poisson problem. We use an FFT (or DCT) to invert the Poisson problem (Sec. 4.1) using eigenvalues  $\tilde{\lambda}_v$  of the discrete Laplacian for discretely divergence free velocity fields (Eq. (17), App. E).

---

**Algorithm 3** Divergence free constraint

---

```

1: function PRESSUREPROJECT( $\psi$ )
2:   for each  $vw \in \mathcal{E}$  do       $\triangleright$  Scaled velocity 1-form at edges
3:      $\tilde{\eta}_{vw} = \arg\langle\psi_v, \psi_w\rangle_{\mathbb{C}}$            $\triangleright \hbar^{-1}$  multiple of Eq. (4)
4:   end for
5:   for each  $v \in \mathcal{V}$  do       $\triangleright$  Scaled divergence at vertices
6:      $\xi_v = \frac{1}{V_v} \sum_{vw \in \mathcal{E}} \frac{A_{vw}}{l_{vw}} \tilde{\eta}_{vw}$            $\triangleright$  Eq. (5)
7:   end for
8:    $\hat{\xi} \leftarrow \text{FFT3D}(\xi)$ 
9:    $\hat{\xi} \leftarrow \hat{\xi} \begin{cases} \tilde{\lambda}^{-1} & \text{if } \tilde{\lambda} \neq 0 \\ 0 & \text{otherwise} \end{cases}$ 
10:   $q \leftarrow \text{INVFFT3D}(\hat{\xi})$ 
11:  return  $e^{-id}\psi$ 
12: end function

```

---

This completes the description of the basic algorithm. While we make extensive use of the FFT (or DCT) our method is not tied to the Fourier domain. For example, the Schrödinger integration could use [Al-Mohy and Higham 2011] while the pressure projection step might employ [McAdams et al. 2010].

Fig.	resolution	size [ $\text{m}^3$ ]	$dt[\text{s}]$	$\hbar[\text{m}^2 \text{s}^{-1}]$	Video
1	$128^3$	$5^3$	$1/48$	0.03	04:48
4	$128 \times 64 \times 64$	$10 \times 5 \times 5$	$1/24$	0.1	00:05
5	$64^3$	$2^3$	$1/24$	0.01	01:17
6	$128^3$	$4^3$	$1/48$	0.02	01:42
7	$128 \times 64 \times 64$	$4 \times 2 \times 2$	$1/48$	0.02-0.04	02:18
8	$192 \times 64 \times 64$	$6 \times 2 \times 2$	$1/48$	0.015	03:41
9	$192 \times 64 \times 64$	$6 \times 2 \times 2$	$1/48$	0.015	03:56
10	$96 \times 192 \times 96$	$3 \times 6 \times 3$	$1/48$	0.02	04:09
13	$128^3$	$4^3$	$1/48$	0.02	02:00
14	$64^3$ resp. $128^3$	$5^3$	$1/24$	0.05	00:39
15	$512 \times 12 \times 208$	$20 \times 1/2 \times 8$	$1/48$	0.03	02:48

Table 2: Parameters for simulations.

### 3 Using the Algorithm

With the basic algorithm in place, we now discuss its use, beginning with simple benchmark simulations and building up a set of straightforward tools capable of describing a large set of interesting simulation scenarios. All examples used our native implementation in **Houdini 15** (Fig. 3). Complete source code is included. Comparisons with other methods used Houdini as well. Performance is controlled by the cost of the FFT. A single step of Alg. 1 takes less than 1s at  $128^3$  resolution and less than 9s at  $256^3$  on a 3.5GHz i7 iMac.

**Note on initializations** ISF is invariant under unitary transformations of  $\mathbb{C}^2$ . We exploit this by initializing  $\psi_1$  with the desired initial state, using  $\psi_2 = \epsilon$  (we use  $\epsilon = 0.01$ ) merely to guard against zeros in  $\psi_1$  during normalization. After normalization simple quantitative statements such as “the norm of  $\psi_2$  indicates the presence of a vortex core” make sense.

#### 3.1 Vortex Filaments

In ISF vorticity has the tendency to concentrate in one-dimensional filaments, as it does in actual fluid dynamics. The ability to create and handle filaments gracefully, inherited from its origins in the theory of superfluids, is a principal strength of ISF. To

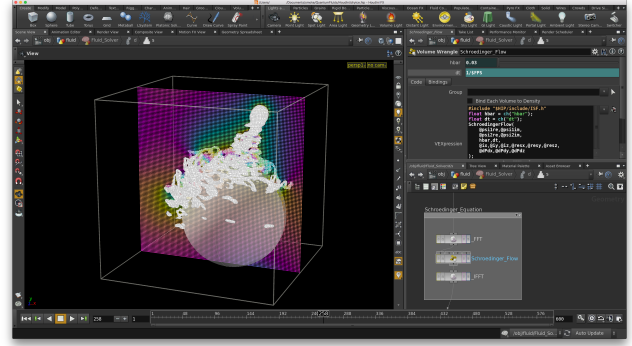


Figure 3: All algorithm components were implemented entirely within Houdini 15.

elucidate this, we look at the way individual filaments evolve and interact in our algorithm. To do so we need a  $\psi^{(0)}$  which represents one or more vortex filaments. Since  $\psi$  for multiple filaments are just the componentwise product of single filament  $\psi$  functions, we begin by describing a simple method for the construction of  $\psi^{(0)}$  for a single filament curve  $\gamma$ .

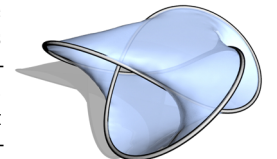
Suppose  $\gamma$  is the boundary of an embedded topological disk,  $\gamma = \partial \Sigma$ . We first construct a complex function  $\varphi$  which has  $\gamma$  as its zero set. Consider the volume created by a positive and negative offset of the oriented surface  $\Sigma$  along its normal direction for distance  $r > 0$  (see inset). In this “slab” of thickness  $2r$  with  $\Sigma$  as its middle surface, set

$$\theta = \pi \left( 1 + \frac{d}{r} \right)$$

for  $d$  the signed distance function of  $\Sigma$ . Letting  $\theta = 0$  outside the slab, we set  $\varphi = e^{i\theta}$ . Pointwise normalizing and pressure projecting  $(\varphi, \epsilon)^\top$  then gives us the desired  $\psi^{(0)}$ , encoding the Biot-Savart velocity field of the curve  $\gamma$ .

A classic example of interesting filament dynamics are the leapfrogging vortex rings [Lim 1997, [Video](#)]. Two closely spaced circular vortex filaments will alternately leapfrog one another. This phenomenon is typically very hard to reproduce in standard fluid solvers but runs without difficulty in our method. Fig. 4 shows a comparison between a state of the art 5<sup>th</sup> order HJWENO [Osher and Fedkiw 2003, Ch. 3.4] velocity advection method with 2<sup>nd</sup> order MacCormack time stepping [Selle et al. 2008], as implemented in Houdini, and our ISF HJWENO/MacCormack is never able to complete even the first leapfrog cycle, quickly yielding only a merged, single vortex ring while our method goes through the correct cycle and is still proceeding without any “damage” after 2000 time steps (approx. four cycles). See also Sec. 4.5 for a discussion of the energy behavior during this simulation.

This method also works for far more complex filaments since there always exists a *Seifert surface*, i.e., an embedded, oriented surface  $\Sigma$ , which is bounded by the closed curve  $\gamma$  [Seifert 1935]. Software to construct it is readily available ([SeifertView](#)). The inset shows the Seifert surface for the trefoil knot. Producing  $\psi^{(0)}$  as above with this  $\Sigma$  we can simulate the evolution of the trefoil knot



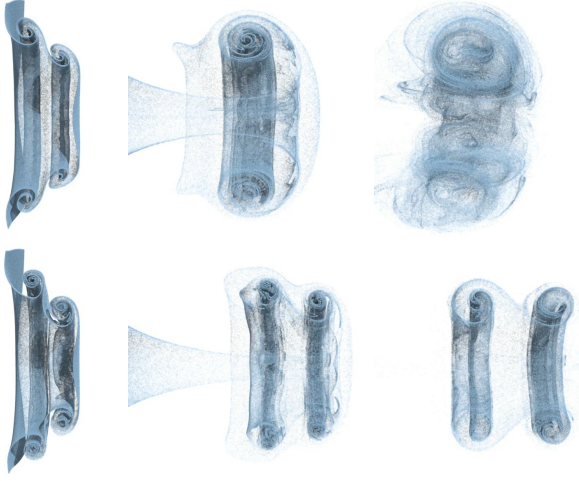


Figure 4: Leapfrogging vortex rings using HJWENO/MacCormack (top) and ISF (bottom). Left to right: iteration 45, 360, 2000 (cmp. to [Lim 1997, [Video](#)]).

(Fig. 5) and correctly replicate the reconnection event which occurs when the initial filament crosses itself. This produces two separate filaments with the smaller one moving off and matches experiments [Kleckner and Irvine 2013, [Video](#)].



Figure 5: Evolution of the trefoil knot with ISF showing frames 50, 100, 210 (cmp. to [Kleckner and Irvine 2013, [Video](#)]).

Taken to an extreme we can produce initial configurations of vortex filaments which optimally approximate arbitrary initial velocity fields using the method of Weißmann and co-workers [2014]. Given a target velocity 1-form  $\hat{\eta}$  a single component wave function  $\varphi$  is found as the ground state of the magnetic Schrödinger operator

$$\varphi = \operatorname{argmin}_{\|\phi\|^2=1} \|d\phi - i\hat{\eta}\phi\|^2,$$

which amounts to finding the principal eigenvector of a SPD matrix. Pointwise normalizing,  $(\varphi/|\varphi|, \epsilon)^\top$ , yields the desired  $\psi^{(0)}$  after pressure projection.

### 3.2 Velocity Constraints

Being able to prescribe a constant velocity in a particular region is a basic tool for the construction of initial conditions as well as while a simulation is running. In the context of our wave function  $\psi$  this amounts to enforcing a *plane wave* in a particular region. Given a wave vector  $k \in \mathbb{R}^3$ , a plane wave is given by the function

$$\varphi^{k,t,\hbar} = e^{i(k,x-\hbar kt/2)}.$$

$\psi^{(0)} = (\varphi^{k,t,\hbar}, 0)^\top$  is then a solution of ISF corresponding to the constant velocity field  $v = \hbar k$ .

Consider now the scenario of setting up an initial, divergence free, velocity field with two regions, say the Bunny and the Teapot, each having some constant but different velocity, e.g., pointing at one another. Using the corresponding  $\psi^{(0)}$  as initial condition, we can simulate the consequent inertial motion dynamics (Fig. 6).

Formally, we seek a divergence free  $\psi$ , constrained to have  $\eta_\Omega$  in some region  $\Omega \subset M$

$$\eta|_\Omega = \eta_\Omega \quad \text{and} \quad *d*\eta = 0.$$

In our example  $\Omega$  would have two connected components, Bunny resp. Teapot, and  $\eta_\Omega$  correspondingly specify a velocity for each component. We construct such an  $\eta$  through *constraint projection*, which enforces the velocity constraint and subsequently ensures vanishing divergence through pressure projection.

---

#### Algorithm 4 Velocity constraint projection

---

```

1: function CONSTRAINTPROJECTION( $\psi, \Omega, k, \hbar, t$ )
2:    $\psi^{\text{tmp}} \leftarrow \psi$ 
3:    $\psi^{\text{tmp}}|_\Omega \leftarrow \varphi^{k,t,\hbar}(|\psi_1|, |\psi_2|)^\top$ 
4:   return PRESSUREPROJECT( $\psi^{\text{tmp}}$ )
5: end function

```

---

Starting with an initial guess, e.g.,  $\psi = (1, \epsilon)^\top$  in  $M \setminus \Omega$  and  $(\varphi^{k_\Omega, t, \hbar}, \epsilon)^\top$  in  $\Omega$  and normalizing it, iterating Alg. 4 is guaranteed to converge [Cheney and Goldstein 1959]. We find that 5 – 10 iterations are sufficient in practice.

Suppose now that we want to simulate a jet. This is an example of enforcing a fixed velocity in some region  $\Omega$ , the jet nozzle, *throughout* the simulation (Fig. 7). To accomplish this we use the *volume penalization* method [Arquis and Caltagirone 1984]. This method was devised for standard fluid simulation methods and includes the constraint via a parameter  $\alpha$  in the Navier-Stokes equation

$$\dot{\eta} + \mathcal{L}_v \eta = v \Delta \eta - dp - \frac{1}{\alpha} \chi_\Omega (\eta - \eta_\Omega) \quad \text{and} \quad *d*\eta = 0.$$

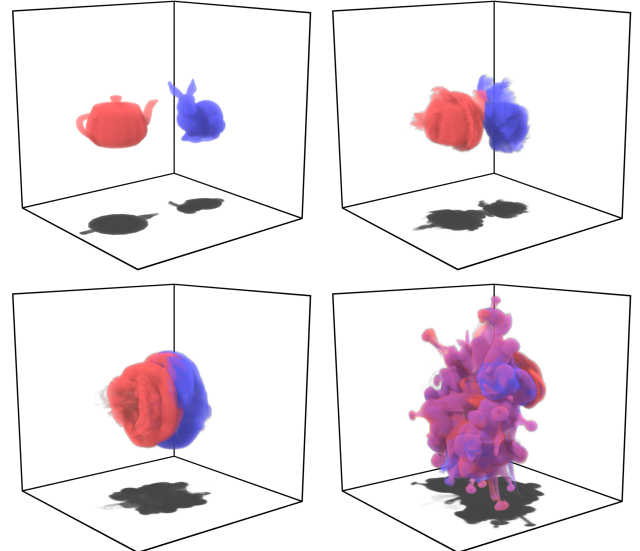


Figure 6: Two regions of red and blue ink are initialized to constant velocities pointing towards each other. Running ISF with this initial condition produces the corresponding inertial motion dynamics (left to right, top to bottom) at frames 1, 25, 85, and 270. The Bunny and Teapot centers were 2m apart, each moving towards the other at  $1\text{m s}^{-1}$ .



Figure 7: Jet of  $1\text{m s}^{-1}$  velocity and a nozzle opening radius of  $0.3\text{m}$ . Left to right the vorticity quantization parameter  $\hbar = 0.04, 0.03, 0.02\text{m}^2\text{s}^{-1}$ , illustrating the finer detail with decreasing  $\hbar$  due to more plentiful and narrowly spaced vortex filaments. The bottom row visualizes filaments as level set surfaces  $|\psi_1|^2 - |\psi_2|^2 = 0$ .

Here  $\nu$  is the kinematic viscosity and  $\chi_\Omega$  the characteristic function of  $\Omega$ . For  $\alpha \rightarrow 0$  the solution converges to a solution of the Navier-Stokes equation which respects the constraints [Angot et al. 1999; Carbou and Fabrie 2003].

To integrate the constraint we use the implicit Euler scheme of [Jause-Labert et al. 2012] as it applies to our  $\psi$ . The method has no time step restriction and we can take the limit of  $\alpha \rightarrow 0$  directly. It amounts to a single constraint projection with parameters at the *end* of the time step, i.e.,  $\psi^{(j+1)}, \Omega^{(j+1)}, k^{(j+1)}, t^{(j+1)}$ . The corresponding call to Alg. 4 follows the pressure projection in Alg. 1.

Fig. 7 shows the resulting simulation also illustrating the effect of different values for  $\hbar$ . With decreasing  $\hbar$  the strength of vortex filaments is lowered and correspondingly their number increased, resulting in finer details in the flow. This can also be seen in the direct visualization of the filaments as level set surfaces.

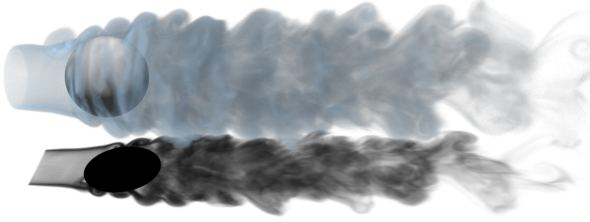


Figure 8: Frame 600 of a spherical obstacle of radius  $0.4\text{m}$  in a  $1\text{m s}^{-1}$  flow.

Maintaining a velocity constraint for some region can also be used to incorporate obstacles into our simulation. In that case  $\eta_\Omega = 0$  while  $\Omega$  may or may not be a function of time. Fig. 8 shows an example of a stationary obstacle in a background flow while Fig. 9 shows a moving obstacle.

### 3.3 Gravity and Buoyancy

Both gravity and buoyancy are important forces in simulations. A simple model for this is the heavy/buoyant vortex filament [Saffman 1992, Sec. 5.8]. Given the way we have initialized  $\psi^{(0)}$ , filaments are zeros of  $\psi_1$  while  $\psi_2$  is indicative of the filament core. Hence buoyancy and gravity enter at the level of the Schrödinger equation (1) as linearly varying potentials applied to the  $\psi_2$  component

$$i\hbar\dot{\psi} = -\frac{\hbar^2}{2}\Delta\psi + p\psi + (0, \langle g, x \rangle \psi_2)^\top,$$

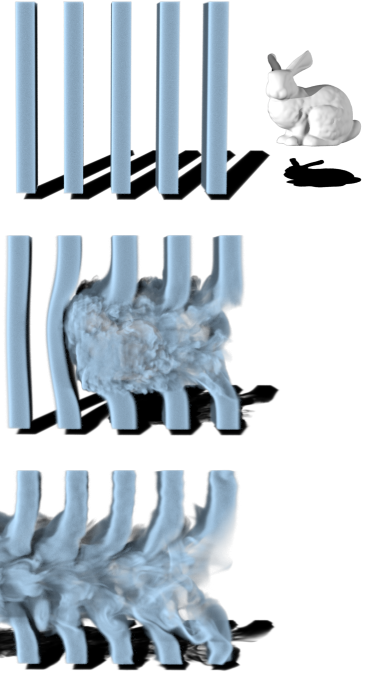


Figure 9: Example of a moving obstacle at frames 1, 100, and 240.

with the vector  $g \in \mathbb{R}^3$  controlling magnitude and direction while  $x \in \mathbb{R}^3$  is the spatial coordinate.

Since the potential does not depend on time, integration is straightforward and amounts to multiplying  $\psi_2$  with the plane wave  $\varphi^{dtg, 0, \hbar}$  after normalization but before pressure projection in Alg. 1.

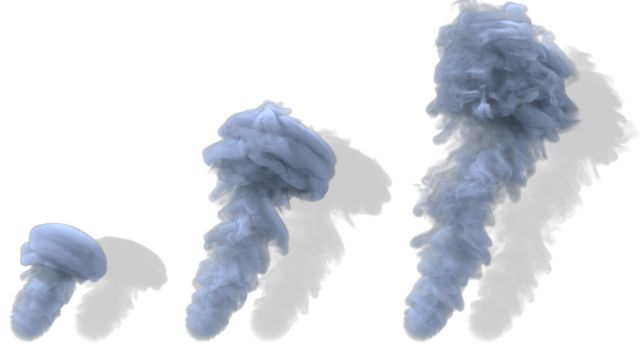


Figure 10: A jet subject to a buoyancy force which “bends” it upwards from its tilted initial trajectory at frame 150, 350, and 500.

Fig. 10 shows an example of a jet with buoyancy causing a gentle upward bend.

## 4 Mathematical Foundations of ISF

To understand ISF we first show that it gives rise to a *Clebsch variable* and then derive the underlying dynamics in terms of this variable. Throughout this section we will identify  $\mathbb{C}^2$  with the quaternions  $\mathbb{H}$ , which greatly simplifies the derivations. Before diving in, we briefly recall some relevant facts regarding Clebsch variables and quaternions. To keep the presentation simple we

assume henceforth that  $M$  is a compact contractible domain in  $\mathbb{R}^3$  with smooth boundary.

**Clebsch variables** represent incompressible flows through a function rather than directly as a velocity or vorticity vector field [Clebsch 1859] (see also [Deng et al. 2005] and references therein for a contemporary exposition). For a flow described by a vorticity 2-form  $\omega$ , a function  $c: M \rightarrow \Sigma$ , for some 2-dimensional manifold  $\Sigma$  equipped with an area form  $dA_\Sigma$ , is called a Clebsch variable if

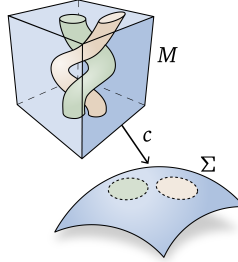
$$\omega = c^* dA_\Sigma$$

where  $c^* dA_\Sigma$  denotes the pull back of the area form. In other words, for each oriented surface  $\Omega \subset M$  with its corresponding image  $c(\Omega) \subset \Sigma$  we have

$$\int_{\Omega} \omega = \int_{c(\Omega)} dA_\Sigma = \text{Area}_\Sigma(c(\Omega)).$$

The preimage of a region in  $\Sigma$  is a *vortex tube* in  $M$  with a vorticity flux cross section constant *along* the tube, and  $c$  serving as a local parameterization of the vortex lines within. In a classical Euler fluid, the dynamics are then characterized by  $c$  being advected by the velocity field

$$\dot{c} + \mathcal{L}_v c = 0. \quad (6)$$



This is typically done for maps to  $\Sigma = \mathbb{R}^2$ , but works equally well for maps to the sphere  $\Sigma = \mathbb{S}^2$  [Kuznetsov and Mikhailov 1980].

**Quaternions** Throughout this section  $\psi \in \mathbb{C}^2$  will be treated as a quaternion via the map  $\psi \mapsto \psi_1 + \psi_2 j$ , where  $j$  is one of the quaternionic imaginary units, the others being  $i$  and  $k$ . At times we also exploit that the imaginary quaternions  $\text{Im } \mathbb{H}$  are in a natural one-to-one correspondence with 3-vectors in  $\mathbb{R}^3$ ,  $(x, y, z) \leftrightarrow xi + yj + zk$ . A quaternion can be thought of as the sum of a scalar and a vector  $a = a_s + a_v = \text{Re}(a) + \text{Im}(a)$ , in terms of which multiplication becomes

$$ab = (a_s b_s - \langle a_v, b_v \rangle) + (a_s b_v + b_s a_v + a_v \times b_v).$$

Lastly for  $|a|^2 = 1$  the product  $\bar{a} b_v a$  represents a general 3D rotation of a 3-vector  $b_v \in \text{Im } \mathbb{H}$  [Cayley 1845]. For a more detailed introduction to quaternions see [Hanson 2005].

To simplify the derivations we use the shorthands

$$\tilde{\eta} := \eta/\hbar = \text{Re}(-\bar{\psi} id\psi), \quad s := \bar{\psi} i\psi, \quad (7)$$

and

$$\begin{aligned} \mu &:= -\bar{\psi} id\psi = \underbrace{\frac{1}{2} (d\bar{\psi} i\psi - \bar{\psi} id\psi)}_{=\text{Re}(d\bar{\psi} i\psi) = \langle d\psi, i\psi \rangle_{\mathbb{R}}} - \underbrace{\frac{1}{2} (d\bar{\psi} i\psi + \bar{\psi} id\psi)}_{=d(\bar{\psi} i\psi) = ds} \\ &= \tilde{\eta} - \frac{1}{2} ds, \end{aligned} \quad (8)$$

in terms of which we may write

$$d\psi = i\psi \left( \tilde{\eta} - \frac{1}{2} ds \right) \quad \text{and} \quad ds = 2(\bar{\psi} id\psi + \tilde{\eta}). \quad (9)$$

#### 4.1 Incompressible $\psi$

Let  $\psi: M \rightarrow \mathbb{C}^n$  be a wave function and  $\rho = |\psi|^2$  its density. For incompressibility we require constant density  $\rho = 1$  and vanishing divergence,  $*d*\eta = 0$ .

The normalization constraint is easily enforced initially for  $n \geq 2$  since a  $\mathbb{C}^2$ -valued function generically never vanishes on a region in  $\mathbb{R}^3$ . Thereafter the constraint  $*d*\eta = 0$  maintains the pointwise normalization (App. A). It is equivalent to  $\langle \Delta\psi, i\psi \rangle_{\mathbb{R}} = 0$  for  $\Delta = *d*d$  since  $\langle d\psi, id\psi \rangle_{\mathbb{R}} = 0$ . Therefore the dynamics of ISF correspond to trajectories  $\psi^{(t)}$  on the manifold

$$\mathcal{M} := \{ \psi \in C^\infty(M, \mathbb{C}^2) \mid |\psi| = 1, \langle \Delta\psi, i\psi \rangle_{\mathbb{R}} = 0, d\psi(N) = 0 \}.$$

Here  $N$  is the unit normal vector field to the boundary of  $M$  and  $d\psi(N) = 0$  is equivalent to the velocity being tangent to  $\partial M$ .

To project an arbitrary  $\psi \in C^\infty(M, \mathbb{C}^2)$  with  $|\psi|^2 = 1$  to  $\mathcal{M}$  observe that for a smooth function  $q: M \rightarrow \mathbb{R}$ ,  $e^{-iq}\psi$  has velocity 1-form  $\eta - \hbar dq$ . Therefore the velocity field will be divergence free if  $q$  satisfies the Poisson problem

$$\Delta q = *d*\tilde{\eta}. \quad (10)$$

Because constant functions form the kernel of  $\Delta$ ,  $e^{-iq}\psi$  is unique up to a global phase, which leaves  $\eta$  unchanged. In the time dependent setting the divergence free constraint is enforced by the potential  $p$  in Eq. (1) (App. A).

#### 4.2 Coordinates on Phase Space

For a proper phase space we need to eliminate the global phase degree of freedom left in the definition of  $\mathcal{M}$  (Sec. 4.1). This is accomplished by using  $s \in C^\infty(M, \mathbb{S}^2)$  as given in Eq. (7).

To see that  $s$  uniquely describes the state of the system, suppose  $\psi, \phi \in \mathcal{M}$  with  $\psi i\psi = s = \phi i\phi$  then there is a function  $q: M \rightarrow \mathbb{R}$  such that  $\phi = e^{-iq}\psi$ . Since  $\psi, \phi \in \mathcal{M}$ ,  $q$  is harmonic with zero Neumann boundary conditions, so in particular  $q$  is constant and  $\psi$  and  $\phi$  are the same element of  $\mathcal{M}$  (up to a global phase). The map  $a \mapsto \bar{a}a$  from  $\mathbb{S}^3$  to  $\mathbb{S}^2$  is known as the Hopf map [Hopf 1931; Lyons 2003].

We have shown that every  $\psi \in \mathcal{M}$  is uniquely determined up to a constant phase by the map  $s = \bar{\psi} i\psi$ . Conversely, using the contractibility of  $M$ , it can be shown that for every  $s \in C^\infty(M, \mathbb{S}^2)$  there is a  $\psi \in \mathcal{M}$  such that  $s = \bar{\psi} i\psi$ .

Thus  $s$  alone represents the state of the system and to study the dynamics of  $\psi$  it suffices to look at the dynamics of  $s \in C^\infty(M, \mathbb{S}^2)$ .

#### 4.3 The Clebsch Variable $s$

Since  $s$  completely describes  $\psi \in \mathcal{M}$  we can study the dynamics of  $\psi^{(t)} \in \mathcal{M}$  under ISF by looking at the time evolution of  $s \in C^\infty(M, \mathbb{S}^2)$ .

**Theorem 1.** *The function  $s = \bar{\psi} i\psi$  is a Clebsch variable of ISF with*

$$\omega = \frac{\hbar}{2} s^* dA_{\mathbb{S}^2} \quad (11)$$

where  $dA_{\mathbb{S}^2}$  is the standard area form on the unit sphere.

*Proof.* To see that the vorticity 2-form of ISF,  $\omega = d\eta = \hbar d\mu$ , can be expressed as the area form on  $\mathbb{S}^2$  first observe that

$$s d\mu = \underbrace{-\bar{\psi} i\psi d\bar{\psi} \wedge id\psi}_{=-d\bar{\psi} \bar{\psi}} = \bar{\psi} id\psi \wedge \bar{\psi} id\psi = \mu \wedge \mu = \frac{1}{4} ds \wedge ds,$$

where the last equality follows from distributing the wedge product over  $\mu = \tilde{\eta} - \frac{1}{2} ds$  (8). Because  $s$  takes on values in  $\mathbb{S}^2$  we have  $ds \wedge ds = 2s(s^* dA_{\mathbb{S}^2})$ . Explicitly, for  $X, Y \in TM$ ,

$$s^* dA_{\mathbb{S}^2}(X, Y) = dA_{\mathbb{S}^2}(ds(X), ds(Y)) = \frac{1}{2} \langle s, ds \times ds \rangle(X, Y).$$

where the cross product of two  $\mathbb{R}^3$ -valued 1-forms  $\alpha$  and  $\beta$  is given by  $\alpha \times \beta(X, Y) = \alpha(X) \times \beta(Y) - \alpha(Y) \times \beta(X)$ . This completes our claim.  $\square$

#### 4.4 Dynamics of the Clebsch Variable

To derive the dynamics of ISF in terms of  $s$  we show that the symplectic gradient flow of the Hamiltonian

$$H_{\text{ISF}}(\psi) = \frac{\hbar^2}{2} \|d\psi\|^2 = \frac{1}{2} \|\eta\|^2 + \frac{\hbar^2}{8} \|ds\|^2 = H_e(\psi) + \frac{\hbar^2}{4} H_s(\psi)$$

(cf. Eq. (3)) coincides with the time evolution of  $s$  when derived directly from the ISF. (Note that the decomposition into kinetic and scaled Dirichlet energies follows directly from Eq. (9).)

First we define a suitable symplectic form on the space of variations of  $s \in C^\infty(M, \mathbb{S}^2)$ . Let  $\dot{s}, \ddot{s} \in T_s C^\infty(M, \mathbb{S}^2)$  be two such variations then

$$\sigma(\dot{s}, \ddot{s}) = \frac{\hbar}{2} \int_M \langle \dot{s}, \dot{s} \times \ddot{s} \rangle$$

is our symplectic form. Next we compute the symplectic gradients of the two terms in the Hamiltonian beginning with the kinetic energy.

Let  $d\Phi = * \eta$  with  $\Phi|_{\partial M} = 0$ , the existence of which is assured by the Helmholtz-Hodge decomposition for manifolds with boundary [Schwarz 1995], and consider a variation  $\dot{s}$  of  $s \in C^\infty(M, \mathbb{S}^2)$

$$\begin{aligned} dH_e(\dot{s}) &= \int_M \dot{\eta} \wedge * \eta = \int_M \dot{\eta} \wedge d\Phi = \int_M -d(\dot{\eta} \wedge \Phi) + d\dot{\eta} \wedge \Phi \\ &= \frac{\hbar}{4} \int_M \left( \underbrace{\langle \dot{s}, ds \times ds \rangle}_{=0} + 2 \langle s, d\dot{s} \times ds \rangle \right) \wedge \Phi \\ &= \frac{\hbar}{2} \int_M d(\langle s, \dot{s} \times ds \rangle \wedge \Phi) - \underbrace{\langle ds, \dot{s} \times ds \rangle}_{=0} \wedge \Phi + \langle s, \dot{s} \times ds \rangle \wedge * \eta \\ &= \frac{\hbar}{2} \int_M \langle s \times \dot{s}, ds \wedge * \eta \rangle = \sigma(\dot{s}, \mathcal{L}_v s). \end{aligned}$$

Here we used Stokes' theorem,  $\Phi|_{\partial M} = 0$ , cyclic permutation in the determinant,  $ds, \dot{s}(p) \in T\mathbb{S}^2$ ,  $s \perp T\mathbb{S}^2$ , and  $*(ds \wedge * \eta) = \mathcal{L}_{\eta^\sharp} s$ .

Recalling that the symplectic gradient  $\text{sgrad}H_e$  is defined by  $\sigma(\dot{s}, \text{sgrad}H_e) = dH_e(\dot{s})$ , we have shown that the Hamiltonian flow of  $H_e$  is

$$\dot{s} = -\text{sgrad}H_e = -\mathcal{L}_v s$$

which establishes Eq. (6) for the Clebsch variable  $s$  and by implication that  $\eta$  behaves as an ideal fluid *modified* by the term arising from the second part of the Hamiltonian, the scaled Dirichlet energy  $H_s$ .

Once again let  $\dot{s}$  be a variation of  $s \in C^\infty(M, \mathbb{S}^2)$

$$\begin{aligned} \frac{\hbar^2}{4} dH_s(\dot{s}) &= \frac{\hbar^2}{4} \int_M \langle d\dot{s} \wedge *ds \rangle = \frac{\hbar^2}{4} \int_M d(\dot{s}, *ds) - \langle \dot{s}, d*ds \rangle \\ &= -\frac{\hbar^2}{4} \int_M \langle s \times \dot{s}, s \times *ds \rangle = -\frac{\hbar}{2} \sigma(\dot{s}, s \times \Delta s), \end{aligned}$$

where we used that the restriction of  $*ds$  to the tangent bundle on the boundary is  $ds(N) dA_{\partial M}$  and  $ds(N) = 0$  since  $d\psi(N) = 0$ .

Consequently the Hamiltonian flow due to  $\frac{\hbar^2}{4} H_s$  is

$$\dot{s} = \frac{\hbar}{2} (s \times \Delta s),$$

the isotropic *Landau-Lifshitz* equation (LLE) [Landau and Lifshits 1935] which describes the evolution of magnetization in ferromagnets with  $s$  giving the orientation (“spin”) of the magnetic field at each point in the domain. Interestingly the LLE by itself admits (magnetic) vortex rings [Cooper 1999; Sutcliffe 2007] which

travel through the material and exhibit such complex dynamics as leapfrogging [Niemi and Sutcliffe 2014].

**Theorem 2.** *ISF is the Hamiltonian flow of  $H_{\text{ISF}} = H_e + \frac{\hbar^2}{4} H_s$ . That is, the evolution of  $s$  under ISF is*

$$\dot{s} + \mathcal{L}_v s = \frac{\hbar}{2} (s \times \Delta s). \quad (12)$$

*Proof.* We compute  $\dot{s}$  directly in terms of  $\psi$  using only  $\psi \in \mathcal{M}$  and that it is a solution of the Schrödinger equation (1)

$$\begin{aligned} \dot{s} &= \bar{\psi} i \psi + \bar{\psi} i \dot{\psi} = 2 \text{Im}(\bar{\psi} i \dot{\psi}) \\ &= 2 \text{Im}(\bar{\psi} i (-\mathcal{L}_v \psi - \frac{\hbar}{4} i \psi (s \times \Delta s) - \tilde{p} i \psi)) \\ &= -(\mathcal{L}_v \bar{\psi} i \psi + \bar{\psi} i \mathcal{L}_v \psi) + \frac{\hbar}{2} (s \times \Delta s) \\ &= -\mathcal{L}_v s + \frac{\hbar}{2} (s \times \Delta s) \end{aligned}$$

where we used Eq. (14) (App. B).  $\square$

As a corollary we find the evolution equation for the velocity 1-form as

$$\dot{\eta} + \mathcal{L}_v \eta = d\hat{p} + \frac{\hbar^2}{4} \langle \Delta s, ds \rangle, \quad *d*\eta = 0$$

for a suitable pressure  $\hat{p}$  (App. C). In particular we see that the velocity 1-form  $\eta$  is advected by the velocity field subject to a tension force.

#### 4.5 Landau-Lifshitz Modified Fluid

In Sec. 4.4 we showed that the dynamics of ISF arise from the standard kinetic energy of  $\eta$ , which would correspond to an ideal fluid, with an  $\frac{\hbar^2}{4}$ -multiple of the Dirichlet energy of  $s$  added in. The latter by itself would have resulted in Landau-Lifshitz dynamics. What is the impact of this modification from the point of view of incompressible fluid simulation? We begin with some basic observations.

For initial data as we set up, almost all the mass of  $\psi$  is contained in  $\psi_1$  over most of the domain. Only near the zero set of  $\psi_1$ , which generically consists of closed curves or curves beginning and ending on the boundary, does  $\psi_2$  take up significant mass due to the normalization constraint  $|\psi|^2 = 1$ . Since  $s_x = |\psi_1|^2 - |\psi_2|^2$  for  $s = \bar{\psi} i \psi$ ,  $s$  is mostly near  $(1, 0, 0)$  and moves towards the antipode  $(-1, 0, 0)$  only near zeros of  $\psi_1$ , inbetween “sweeping” over the entire sphere  $\mathbb{S}^2$  (Fig. 11). Eq. (11) then implies that the vorticity integral over a small surface transversal to a zero set of  $\psi_1$  is  $2\pi\hbar$ . In particular, filaments in ISF carry vorticity quantized to  $2\pi\hbar$ .

This characterization of  $s$  continues to hold as the simulation progresses since the mean of  $s$  is an invariant of the flow. This follows from  $\|\psi_1\|^2$  and  $\|\psi_2\|^2$  being invariants since  $\psi_1$  and  $\psi_2$  by themselves are solutions to the Schrödinger equation, whose time evolution is unitary. Hence the mean of  $s_x$  is invariant. Due to the symmetry of  $\mathbb{S}^2$  so must be the mean of  $s$ .

But what does this imply for the Landau-Lifshitz energy? Since the Dirichlet integrand is bounded below by the absolute value of the area density, Eq. (11) implies

$$\frac{1}{2} |ds|^2 \geq \frac{2}{\hbar} |\omega|,$$

with equality achieved for a conformal map  $s$ . Here  $|\omega|$  is the norm of the corresponding vorticity vector field. In practice we observe that the Landau-Lifshitz energy is *near* this minimum and hence the Dirichlet integrand supported mostly in the vicinity of

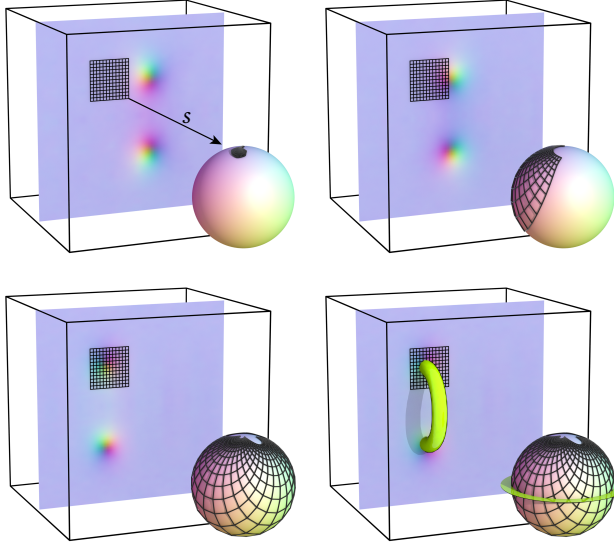


Figure 11: A slice of a 3D domain with a vortex filament moving to the left. The color on the plane visualizes  $s$  according to the color map on the sphere. Large regions of the plane are nearly the same color, i.e., covering a small area on the sphere = little vorticity. As the filament translates the gridded region maps to an ever larger area on the sphere (see also Fig. 7).

the filaments, with an integral over a surface transversal to the filament yielding approximately  $2\pi\hbar$  independent of the thickness of the filament. Consequently, the integral of the Dirichlet energy for a tubular neighborhood of a filament  $\gamma$  yields  $\approx 4\pi L(\gamma)$ .

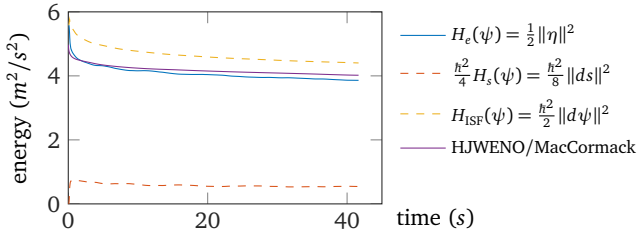


Figure 12: Energy plot for the leapfrogging vortex filaments (Fig. 4). The kinetic energy tracks closely between HJWENO/MacCormack and ISF. The additional Landau-Lifshitz component in the latter stays nearly constant, keeping the vortex filaments “alive” in ISF.

What then are the dynamics consequences of the Landau-Lifshitz energy term? In examples of ISF we observe phenomena which are difficult to reproduce using grid simulations without excessively high resolution (Figs. 4, 13, 14). Since such phenomena arise from vortex filaments whose thickness is comparable to the grid resolution, a velocity or vorticity representation of fluids tends to lose the energy contained in the vortex cores, directly impacting the dynamics of the coherent vortical structures. For ISF the Landau-Lifshitz energy, proportional to the total length of the filaments independent of their thickness, maintains this otherwise lost energy. Fig. 12 demonstrates this quantitatively for the simple example of the leapfrogging vortex filaments of Fig. 4.

Additionally, the length  $L(\gamma)$  of filaments is also the Hamiltonian of the *local induction approximation* (LIA) for the motion of thin vortex filaments [Rios 1906; Hasimoto 1972] (see [Saffman 1992, Ch. 11] for a modern exposition). This hints at a deeper relation between the LIA and the Landau-Lifshitz term in ISF. Fig. 13 shows the simulation of the Teapot/Bunny collision using Eulerian HJWENO/MacCormack (top left) and a Lagrangian filament method [Weißmann and Pinkall 2010] (top center), comparing it to our ISF (top right; see also Fig. 6 bottom right). Remarkably, the Lagrangian filament simulation which uses sub-grid scale vortex thickness and explicitly includes the LIA forces, yields qualitatively the same results as our Eulerian ISF method.

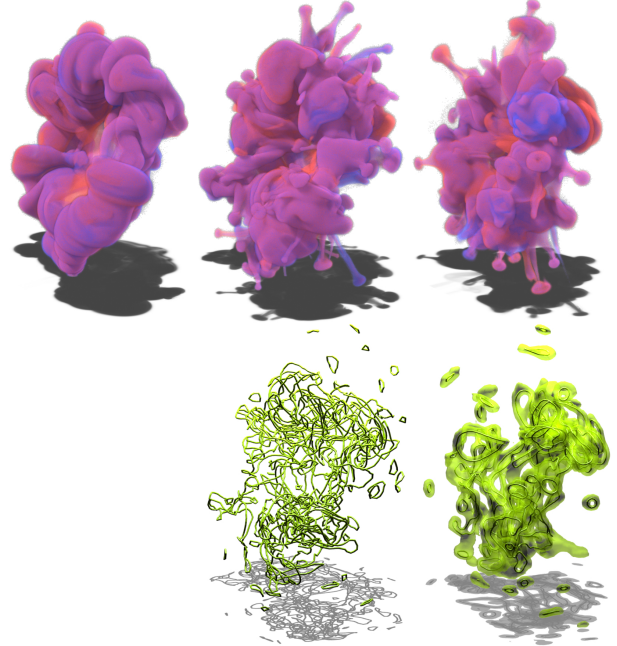


Figure 13: Frame 270 from colliding Teapot/Bunny simulation using Eulerian HJWENO/MacCormack (top left), Lagrangian vortex filaments [Weißmann and Pinkall 2010] (top center), and our Eulerian ISF (top right). The center bottom shows the filaments of Weißmann and Pinkall which, at thickness 0.017m, are below the grid size of the ISF simulation. ISF vortex tubes ( $|\psi_1|^2 - |\psi_2|^2 = 0$ ) and their cores ( $\psi_1 = 0$ ) are shown on the bottom right.

A further example of vortex filament dynamics, which are challenging to simulate, are the obliquely colliding vortex rings [Lim 1989, Videos [front](#) & [top](#)]. Fig. 14 compares our method with stable fluids and HJWENO/MacCormack at two resolutions. Stable fluids, due to its excessive numerical diffusion cannot reproduce this experiment at all. HJWENO/MacCormack does somewhat better and successfully reproduces the reconnection event only at  $256^3$  resolution (not shown). ISF on the other hand produces the correct dynamics already at  $64^3$ .

## 5 Additional Results

An important characterization of classical fluids is given by the *Reynolds number*  $Re = |\nu|D/\mu$  where  $D$  is a characteristic size, e.g., the diameter of an obstacle in a flow,  $|\nu|$  a characteristic speed, e.g., speed of the background flow, and  $\mu$  the kinematic viscosity. For superfluids as well as our setup there is no kinematic viscosity, but one can define an equivalent *superfluid Reynolds*

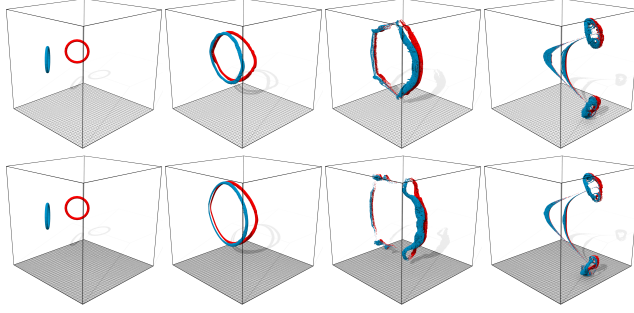


Figure 14: Comparison of methods for oblique smoke ring collision at resolution  $64^3$  (top) and  $128^3$  (bottom) showing from left to right the initial configuration, stable fluids with RK4 back trace, HJWENO/MacCormack, and ISF, each at frame 600. The vortex filaments have strength  $2\pi\hbar$  for  $\hbar = 0.05\text{m}^2\text{s}^{-1}$ , they are of radius 0.6m making an angle of  $\pm 45^\circ$  to the domain with their centers separated by 2m (cmp. to [Lim 1989, Videos *front* & *top*]).

number  $\text{Re}_s = |v|D/(2\pi\hbar)$  [Volovik 2003], where  $|v|/(2\pi\hbar)$  is the number of filaments per unit of distance. Note that the typical range of  $\text{Re}_s$  is quite different from the classical Reynolds number. In our experiments  $1 \leq \text{Re}_s \leq 10$ .

The superfluid Reynolds number is helpful when scaling simulations. For example, scaling  $\hbar$  and the velocity by the same factor leaves  $\text{Re}_s$  invariant.



Figure 15: Von Kármán vortex street forming behind a cylindrical obstacle with  $\text{Re}_s \approx 3.18$  and  $\text{St} \approx 0.14$  at frame 1050. The cylinder measured 0.3m radius in a flow of  $1\text{m s}^{-1}$ .

A phenomenon that is characterized by the Reynolds number is the shedding of vortices with a particular frequency  $f$  from an obstacle. This can be captured by the Strouhal number [Strouhal 1878],  $\text{St} = fD/|v|$ . For a large range of Reynolds numbers ( $\text{Re} \in [800, 200000]$ ) one finds  $\text{St} \approx 0.2$ . Such measurements, though far fewer in number, have also been performed for superfluids (simulation and experiment) where the corresponding Strouhal number falls into the range of  $0.12 - 0.18$  [Reeves et al. 2015]. In our own experiments we have observed  $0.14 \leq \text{St} \leq 0.18$  for  $2 \leq \text{Re}_s \leq 8$  (see Fig. 15 for a typical example). This agrees well with the numbers reported for superfluids and is close to, though smaller than, the universal 0.2 for classical fluids.

## 6 Discussion

ISF is a close relative of the GP equation, replacing the cubic non-linear term with the limiting case of pressure projection to enforce a divergence free velocity field. The corresponding dynamics are related to superfluids but can be used for the visual simulation of classical fluids as we have demonstrated. Because ISF adds a Landau-Lifshitz energy term to what would otherwise have been an Euler fluid, we find that coherent vortical structures and their dynamics are captured, even at modest resolutions, with fidelity rivaling purely Lagrangian methods.

**Shortcomings** There are a number of practical issues and open theoretical questions at this time.

The simple splitting method we employ for time integration exhibits loss of kinetic energy. Even though its impact is not as problematic due to the Landau-Lifshitz term, design of an integrator more tailored to the particulars of ISF would be very interesting.

Design of flows is not yet fully general. For example, we do not know how to express arbitrary forces at the level of  $\psi$ , limiting the use of standard special effects design tools.

With discrete circulation given by the difference of phases along an edge (4), there is an upper bound on the velocity that can be represented without aliasing. Ideas from [Knöppel et al. 2015] may help here. A related issue arises at the global level, where the periodicity of the domain leads to quantization of gravity/buoyancy.

Our method has only one parameter,  $\hbar$ , which controls the quantization of vorticity. Notably there is no parameter to control viscosity, though there are diffusion [Frisch et al. 1992] and drag [Sasaki et al. 2010] phenomena.

The implicit integrator for constraints is of low order, occasionally leading to leakage of fluid into the interior of obstacles. A higher order integrator for the constraints would therefore be desirable.

**Open Questions and Opportunities** In this paper we have only scratched the surface of the theory underlying ISF.

An interesting direction to pursue is the simulation of multi-phase fluids, e.g., air and water. When applying gravity/buoyancy forces we have already treated the two components of  $\psi$  differently. How far can this be taken? How do interface forces enter? Are there interesting physics to be modeled with wave functions  $\psi: M \rightarrow \mathbb{C}^n$  for  $n > 2$ ?

At the theory level we would like to understand the limit of  $\hbar \rightarrow 0$ . Does it yield Euler fluids? How can we characterize the velocity fields which can be represented by  $\psi \in \mathcal{M}$  resp.  $s \in C^\infty(M, \mathbb{S}^2)$ ?

Clearly we are only at the beginning of exploring this new approach to fluid simulation and are hopeful that many new mathematical, physical, and simulation tools will spring from it.

## Acknowledgments

This work was supported in part by the DFG Collaborative Research Center TRR 109 “Discretization in Geometry and Dynamics,” Joel A. Tropp under the auspices of ONR grant N00014-11-1-0025, and the German Academic Exchange Service (DAAD). Additional support was provided by IST at Caltech, SideFX software, and Framestore Los Angeles. We also gratefully acknowledge Alessandro Pepe’s help with visualization. The Bunny model is courtesy Stanford Computer Graphics laboratory while the Teapot is courtesy the Computer Graphics program at the University of Utah.

## References

- ABRAHAM, R., MARSDEN, J. E., AND RATIU, T. 2001. *Manifolds, Tensor Analysis and Applications*. No. 75 in Appl. Math. Sci. Springer.
- AL-MOHY, A. H., AND HIGHAM, N. J. 2011. Computing the Action of the Matrix Exponential with an Application to Exponential Integrators. *SIAM J. Sci. Comp.* 33, 2, 488–511.

- ANGELIDIS, A., AND NEYRET, F. 2005. *Simulation of Smoke based on Vortex Filament Primitives*. In *Proc. Symp. Comp. Anim.*, ACM SIGGRAPH/Eurographics, 87–96.
- ANGOT, P., BRUNEAU, C.-H., AND FABRIE, P. 1999. *A Penalization Method to Take into account Obstacles in Incompressible Viscous Flows*. *Numer. Math.* 81, 4, 497–520.
- ARQUIS, E., AND CALTAGIRONE, J.-P. 1984. *Sur les conditions hydrodynamiques au voisinage d'une interface milieu fluide-milieu poreux: application à convection naturelle*. *CR Acad. Sci. Paris, Série II* 299, 1, 1–4.
- BRIDSON, R., HOURIHAM, J., AND NORDENSTAM, M. 2007. *Curl-noise for Procedural Fluid Flow*. *ACM Trans. Graph.* 26, 3, 46:1–3.
- BROCHU, T., KEELER, T., AND BRIDSON, R. 2012. *Linear-Time Smoke Animation with Vortex Sheet Meshes*. In *Proc. Symp. Comp. Anim.*, ACM SIGGRAPH/Eurographics, 87–95.
- CARBOU, G., AND FABRIE, P. 2003. *Boundary Layer for a Penalization Method for Viscous Incompressible Flow*. *Adv. Diff. Eq.* 8, 12, 1453–1480.
- CAYLEY, A. 1845. *On Certain Results Relating to Quaternions*. *Phil. Mag.* 26, 141–145.
- CHENEY, W., AND GOLDSTEIN, A. A. 1959. *Proximity Maps for Convex Sets*. *Proc. AMS* 10, 3, 448–450.
- CLEBSCH, A. 1859. *Ueber die Integration der hydrodynamischen Gleichungen*. *J. Reine Angew. Math.* 56, 1–10.
- COOPER, N. R. 1999. *Propagating Magnetic Vortex Rings in Ferromagnets*. *Phys. R. Lett.* 82, 7, 1554–1557.
- COTTET, G.-H., AND KOUMOUTSAKOS, P. D. 2000. *Vortex Methods: Theory and Practice*. Cam. U. Press.
- CRANE, K., DE GOES, F., DESBRUN, M., AND SCHRÖDER, P. 2013. *Digital Geometry Processing with Discrete Exterior Calculus*. In *Courses*, ACM SIGGRAPH.
- DENG, J., HOU, T. Y., AND YU, X. 2005. *A Level Set Formulation for the 3D Incompressible Euler Equations*. *Methods Appl. Anal.* 12, 4, 427–440.
- DESBRUN, M., KANSO, E., AND TONG, Y. 2008. *Discrete Differential Forms for Computational Modeling*. In *Discrete Differential Geometry*, A. I. Bobenko, P. Schröder, J. M. Sullivan, and G. M. Ziegler, Eds., Vol. 38 of *Oberwolfach Seminars*. Birkhäuser Verlag.
- ELCOTT, S., TONG, Y., KANSO, E., SCHRÖDER, P., AND DESBRUN, M. 2007. *Stable, Circulation-Preserving, Simplicial Fluids*. *ACM Trans. Graph.* 26, 1, 4:1–12.
- FEDKIW, R., STAM, J., AND JENSEN, H. W. 2001. *Visual Simulation of Smoke*. In *Proc. ACM/SIGGRAPH Conf*, ACM, 15–22.
- FEYNMAN, R. P. 1955. *Application of Quantum Mechanics to Liquid Helium*, Vol. 1 of *Progress in Low Temperature Physics*. North-Holland, Ch. II, 17–53.
- FRISCH, T., POMEAU, Y., AND RICA, S. 1992. *Transition to Dissipation in a Model of Superflow*. *Phys. R. Lett.* 69, 11, 1644–1647.
- GINSBURG, V. L., AND PITAEVSKII, L. P. 1958. *On the Theory of Superfluidity*. *J. Exp. Theor. Phys.* 7, 5, 858–861.
- GROSS, E. P. 1961. *Structure of a Quantized Vortex in Boson Systems*. *Il Nuovo Cimento* 20, 3, 454–477.
- HALL, H. E., AND VINEN, W. F. 1956. *The Rotation of Liquid Helium II. II. The Theory of Mutual Friction in Uniformly Rotating Helium II*. *Proc. R. Soc. L. A, Math. Phys. S.* 238, 1213, 215–234.
- HANSON, A. J. 2005. *Visualizing Quaternions*. Morgan Kaufmann.
- HASIMOTO, H. 1972. *A Soliton on a Vortex Filament*. *J. Fl. Mech.* 51, 3, 477–485.
- HOPF, H. 1931. *Über die Abbildungen der Dreidimensionalen Sphäre auf die Kugelfläche*. *Math. Ann.* 104, 1, 637–665.
- JAUSE-LABERT, C., GODEFERD, F. S., AND FAVIER, B. 2012. *Numerical Validation of the Volume Penalization Method in Three-Dimensional Pseudo-Spectral Simulations*. *Comp. & Fl.* 67, 41–56.
- JERRARD, R. L., AND SPIRN, D. 2015. *Hydrodynamic Limit of the Gross-Pitaevskii Equation*. *Comm. Par. Diff. Eq.* 40, 2, 135–190.
- KIM, T., THÜREY, N., JAMES, D., AND GROSS, M. 2008. *Wavelet Turbulence for Fluid Simulation*. *ACM Trans. Graph.* 27, 3, 50:1–6.
- KIM, D., YOUNG SONG, O., AND KO, H.-S. 2009. *Stretching and Wiggling Liquids*. *ACM Trans. Graph.* 28, 5, 120:1–7.
- KLECKNER, D., AND IRVINE, W. T. M. 2013. *Creation and Dynamics of Knotted Vortices*. *Nature Physics* 9, 253–258. Video at <http://www.nature.com/nphys/journal/v9/n4/extref/nphys2560-s7.mov>.
- KNÖPPEL, F., CRANE, K., PINKALL, U., AND SCHRÖDER, P. 2015. *Stripe Patterns on Surfaces*. *ACM Trans. Graph.* 34, 4, 39:1–11.
- KOUMOUTSAKOS, P., COTTET, G.-H., AND ROSSINELLI, D. 2008. *Flow Simulations Using Particles: Bridging Computer Graphics and CFD*. In *ACM/SIGGRAPH Conf. Classes*, ACM/SIGGRAPH, 25:1–25:73.
- KUZNETSOV, E. A., AND MIKHAILOV, A. V. 1980. *On the Topological meaning of Canonical Clebsch Variables*. *Phys. Lett. A* 77, 1, 37–38.
- LANDAU, L., AND LIFSHITS, E. 1935. *On the Theory of the Dispersion of Magnetic Permeability in Ferromagnetic Bodies*. *Phys. Zeitsch. Sow.* 8, 153–169.
- LEONARD, A. 1980. *Vortex Methods for Flow Simulation*. *J. Comput. Phys.* 37, 3, 289–335.
- LIM, T. T. 1989. *An Experimental Study of a Vortex Ring Interacting with an Inclined Wall*. *Exp. in Fl.* 7, 7, 453–463. Videos at [http://serve.me.nus.edu.sg/limtt/video/Obllique\\_collision\\_front.mpg](http://serve.me.nus.edu.sg/limtt/video/Obllique_collision_front.mpg) and [http://serve.me.nus.edu.sg/limtt/video/Obllique\\_collision\\_top.mpg](http://serve.me.nus.edu.sg/limtt/video/Obllique_collision_top.mpg).
- LIM, T. T. 1997. *A Note on the Leapfrogging between two Coaxial Vortex Rings at low Reynolds Number*. *Phys. Fluids* 9, 1, 239–241. Video at <http://serve.me.nus.edu.sg/limtt/video/leapfrog.mpeg>.
- LIN, F.-H., AND XIN, J. X. 1999. *On the Incompressible Fluid Limit and the Vortex Motion Law of the Nonlinear Schrödinger Equation*. *Comm. Math. Phys.* 200, 2, 249–274.
- LYONS, D. W. 2003. *An Elementary Introduction to the Hopf Fibration*. *Math. Mag.* 76, 2, 87–98.
- MADELUNG, E. 1926. *Eine anschauliche Deutung der Gleichung von Schrödinger*. *Nat. Wiss.* 14, 45, 1004–1004.

- MADELUNG, E. 1927. Quantentheorie in hydrodynamischer Form. *Z. Phys.* 40, 3-4, 322–326.
- MCADAMS, A., SIFAKIS, E., AND TERAN, J. 2010. A Parallel Multi-grid Poisson Solver for Fluids Simulation on large Grids. In *Proc. Symp. Comp. Anim.*, ACM SIGGRAPH/Eurographics, 65–74.
- NIEMI, A. J., AND SUTCLIFFE, P. 2014. Leapfrogging Vortex Rings in the Landau-Lifshitz Equation. *Nonlinearity* 27, 9.
- ONSAGER, L. 1949. Statistical Hydrodynamics. *Il Nuovo Cimento* 6, 2, 279–287. Footnote (1).
- OSHER, S., AND FEDKIW, R. 2003. *Level Set Methods and Dynamic Implicit Surfaces*, Vol. 153 of *Appl. Math. Sci.* Springer.
- PACKARD, R. E., AND SANDERS, T. M. 1969. Detection of Single Quantized Vortex Lines in Rotating HE II. *Phys. R. Lett.* 22, 16, 823–826.
- PARK, S. I., AND KIM, M. J. 2005. Vortex Fluids for Gaseous Phenomena. In *Proc. Symp. Comp. Anim.*, ACM SIGGRAPH/Eurographics, 261–270.
- PEAFF, T., THÜREY, N., AND GROSS, M. 2012. Lagrangian Vortex Sheets for Animating Fluids. *ACM Trans. Graph.* 31, 4, 112:1–8.
- PITAEVSKII, L. P. 1961. Vortex Lines in an Imperfect Bose Gas. *J. Exp. Theor. Phys.* 13, 2, 451–454.
- REEVES, M. T., BILLAM, T. P., ANDERSON, B. P., AND BRADLEY, A. S. 2015. Identifying a Superfluid Reynolds Number via Dynamical Similarity. *Phys. R. Lett.* 114, 15, 155302 (5pp).
- RIOS, L. S. D. 1906. Sul moto d'un liquido indefinito con un filetto vorticoso di forma qualunque. *Rend. Cir. Mat. Pal.* 22, 1, 177–135.
- ROSENHEAD, L. 1931. The Formation of Vortices from a Surface of Discontinuity. *Proc. R. Soc. Lond. A* 134, 823, 170–192.
- SAFFMAN, P. G. 1992. *Vortex Dynamics*. Cam. U. Press.
- SASAKI, K., SUZUKI, N., AND SAITO, H. 2010. Bénard – von Kármán Vortex Street in a Bose-Einstein Condensate. *Phys. R. Lett.* 104, 15–16, 150404 (4pp).
- SCHÖNBERG, M. 1954. On the Hydrodynamical Model of the Quantum Mechanics. *Il Nuovo Cimento* 12, 1, 103–133.
- SCHWARZ, K. W. 1985. Three-Dimensional Vortex Dynamics in Superfluid  $^4\text{He}$ : Line-Line and Line-Boundary Interactions. *Phys. R. B* 31, 9, 5782–5804.
- SCHWARZ, G. 1995. *Hodge Decomposition - A Method for Solving Boundary Value Problems*. Springer.
- SEIFERT, H. 1935. Über das Geschlecht von Knoten. *Math. Ann.* 110, 1, 571–592.
- SELLA, A., RASMUSSEN, N., AND FEDKIW, R. 2005. A Vortex Particle Method for Smoke, Water and Explosions. *ACM Trans. Graph.* 24, 3, 910–914.
- SELLA, A., FEDKIW, R., KIM, B., AND ROSSIGNAC, J. 2008. An Unconditionally Stable MacCormack Method. *J. Sci. Comp.* 35, 2–3, 350–371.
- SOROKIN, A. L. 2001. Madelung Transformation for Vortex Flows of a Perfect Liquid. *Doklady Physics* 46, 8, 576–578.
- STAGG, G. W., PARKER, N. G., AND BARENGHI, C. F. 2014. Quantum Analogues of Classical Wakes in Bose-Einstein Condensates. *J. Phys. B: At. Mol. Opt. Phys.* 47, 9, 095304 (8pp).
- STAM, J. 1999. Stable Fluids. In *Proc. ACM/SIGGRAPH Conf.*, ACM, 121–128.
- STEINHOFF, J., AND UNDERHILL, D. 1994. Modification of the Euler Equations for “Vorticity Confinement:” Application to the Computation of Interacting Vortex Rings. *Phys. Fluids* 6, 8, 2738–2744.
- STOCK, M. J., DAHM, W. J. A., AND TRYGGVASON, G. 2008. Impact of a Vortex Ring on a Density Interface using a Regularized Inviscid Vortex Sheet Method. *J. Comput. Phys.* 227, 21, 9021–9043.
- STROUHAL, V. 1878. Ueber eine besondere Art der Tonerregung. *Ann. Ph. Ch., Series III* 5, 10, 216–250.
- SUTCLIFFE, P. 2007. Vortex Rings in Ferromagnets: Numerical Simulations of the Time-Dependent Three-Dimensional Landau-Lifshitz Equation. *Phys. R. B* 76, 18, 184439 (6pp).
- VOLOVIK, G. E. 2003. Classical and Quantum Regimes of Superfluid Turbulence. *JETP Letters* 78, 9, 533–537.
- WEISSMANN, S., AND PINKALL, U. 2010. Filament-Based Smoke with Vortex Shedding and Variational Reconnection. *ACM Trans. Graph.* 29, 4, 115:1–12.
- WEISSMANN, S., PINKALL, U., AND SCHRÖDER, P. 2014. Smoke Rings from Smoke. *ACM Trans. Graph.* 33, 4, 140:1–8.
- ZHANG, X., BRIDSON, R., AND GREIF, C. 2015. Restoring the Missing Vorticity in Advection-Projection Fluid Solvers. *ACM Trans. Graph.* 34, 4, 52:1–8.

## A Pressure Potential

For incompressibility we require constant density  $\rho = |\psi|^2 = 1$  and  $\text{div}(v) = 0$ . When  $\rho = 1$  the constraint  $\text{div}(v) = 0$  is equivalent to  $\langle \Delta\psi, i\psi \rangle_{\mathbb{R}} = 0$ . This condition maintains the pointwise normalization under Eq. (1) since

$$\frac{\partial}{\partial t} |\psi|^2 = 2\langle \dot{\psi}, \psi \rangle_{\mathbb{R}} = -\hbar \langle \Delta\psi, i\psi \rangle_{\mathbb{R}} - \frac{2}{\hbar} p \langle i\psi, \psi \rangle_{\mathbb{R}} = 0.$$

To ensure  $\langle \Delta\psi, i\psi \rangle_{\mathbb{R}} = 0$ , observe that for an arbitrary  $\psi \in C^{\infty}(M, \mathbb{C}^2)$  with  $|\psi|^2 = 1$  there exists a smooth phase  $q: M \rightarrow \mathbb{R}$  so that  $e^{-iq}\psi$  is divergence free (Sec. 4.1). Therefore the term  $p\psi$  in Eq. (1), which generates general phase shifts, suffices to keep  $\psi$  divergence free.

Explicitly, the scalar potential  $p: M \rightarrow \mathbb{R}$  in Eq. (1) ensures a divergence free velocity field when it solves

$$\Delta p = \frac{\hbar^2}{2} (\langle \Delta^2\psi, \psi \rangle_{\mathbb{R}} - \langle \Delta\psi, \Delta\psi \rangle_{\mathbb{R}}) \quad \text{with} \quad \int_M p = 0. \quad (13)$$

To see this, note that  $\langle \Delta\psi, i\psi \rangle_{\mathbb{R}}$  must have vanishing time derivative, yielding

$$\begin{aligned} 0 &= \hbar \frac{\partial}{\partial t} \langle \Delta\psi, i\psi \rangle_{\mathbb{R}} = \langle \Delta\psi, i\hbar\dot{\psi} \rangle_{\mathbb{R}} - \langle \Delta i\hbar\dot{\psi}, \psi \rangle_{\mathbb{R}} \\ &= \langle \Delta\psi, -\frac{\hbar^2}{2} \Delta\psi + p\psi \rangle_{\mathbb{R}} + \langle \frac{\hbar^2}{2} \Delta^2\psi - \Delta(p\psi), \psi \rangle_{\mathbb{R}} \\ &= \frac{\hbar^2}{2} (\langle \Delta^2\psi, \psi \rangle_{\mathbb{R}} - \langle \Delta\psi, \Delta\psi \rangle_{\mathbb{R}}) - \Delta p - 2\langle d\psi(\nabla p), \psi \rangle_{\mathbb{R}}, \end{aligned}$$

which proves Eq. (13) since  $d\psi \perp \psi$  due to  $|\psi|^2 = 1$ .

This  $p$  serves as the Lagrange multiplier for the divergence constraint in the continuous time setting. For discrete time, *i.e.*, at each time step, this role is played by  $q$  of Eq. (10), which pressure projects a given  $\psi$  to the constraint space (Sec. 4.1).

## B Evolution of $\psi$

Here we rewrite the Schrödinger equation to expose the advection going on “under the hood” and we will find that  $\psi$  is  *advected by the velocity field* subject to a modified pressure potential and a *Landau-Lifshitz* term

$$\dot{\psi} + \mathcal{L}_v \psi = -i\psi \left( \frac{\hbar}{4}(s \times \Delta s) + \tilde{p} \right) \quad (14)$$

where  $\tilde{p} = \frac{p}{\hbar} - \frac{\hbar}{2}|d\psi|^2 - \frac{\hbar}{4}\langle s, \Delta s \rangle$ .

Eq. (14) follows from replacing  $\Delta\psi$  in Eq. (1) with

$$\begin{aligned} \Delta\psi &= *d(i\psi(*\tilde{\eta} - \frac{1}{2}*ds)) \\ &= i*(d\psi \wedge *\tilde{\eta}) - \frac{i}{2}*(d\psi \wedge *ds) - \frac{i}{2}\psi \Delta s \\ &= i\mathcal{L}_{\tilde{\eta}^\sharp}\psi + \frac{1}{2}\psi *((\tilde{\eta} - \frac{1}{2}ds) \wedge *ds) - \frac{1}{2}\psi s \Delta s \\ &= \frac{i}{\hbar}\mathcal{L}_v\psi + \psi *(\tilde{\eta} \wedge *(\tilde{\eta} + \bar{\psi}id\psi)) + \frac{1}{4}*(d\tilde{\eta} \wedge *ds) - \frac{1}{2}s \Delta s \\ &= i\frac{2}{\hbar}\mathcal{L}_v\psi + \psi(|\tilde{\eta}|^2 + \frac{1}{4}|ds|^2 - \frac{1}{2}s \Delta s) \\ &= i\frac{2}{\hbar}\mathcal{L}_v\psi + \psi(|\tilde{\eta}|^2 + \frac{1}{4}|ds|^2 + \frac{1}{2}\langle s, \Delta s \rangle - \frac{1}{2}(s \times \Delta s)) \end{aligned} \quad (15)$$

which used Eq. (9),  $*d*\tilde{\eta} = 0$ , the Hermitian product of two quaternionic  $k$ -forms,  $\langle \alpha, \beta \rangle = *(\bar{\alpha} \wedge * \beta)$ , the Lie derivative of a function,  $\mathcal{L}_v\psi = d\psi(v) = *(d\psi \wedge *\eta) = *(\eta \wedge *d\psi)$  for  $v = \eta^\sharp$ , and  $s \Delta s = -\langle s, \Delta s \rangle + s \times \Delta s$ .

## C Evolution of $\eta$

To derive the evolution equation for  $\eta$  we differentiate Eq. (14), multiply the result on the left with  $-\bar{\psi}i$ , and finally take its real part.

We begin with the lhs of Eq. (14)

$$\begin{aligned} -\text{Re}(\bar{\psi}i(d\dot{\psi} + \mathcal{L}_v d\psi)) &= \text{Re}(-\bar{\psi}ii\dot{\psi}\mu + \dot{\mu} - \bar{\psi}i\mathcal{L}_v(i\psi\mu)) \\ &= \text{Re}(\bar{\psi}\dot{\psi}\mu) + \dot{\tilde{\eta}} + \text{Re}(\bar{\psi}\mathcal{L}_v\psi\mu + \bar{\psi}\psi\mathcal{L}_v\mu) \\ &= \text{Re}(\bar{\psi}(-i\frac{\hbar}{4}\psi(s \times \Delta s) + \tilde{p}i\psi)\mu) + \dot{\tilde{\eta}} + \mathcal{L}_v\tilde{\eta} \\ &= \dot{\tilde{\eta}} + \mathcal{L}_v\tilde{\eta} - \frac{\hbar}{8}\langle \Delta s, ds \rangle, \end{aligned}$$

since  $d(\bar{\psi}\psi) = 0 = d\bar{\psi}\psi + \bar{\psi}d\psi$  implies  $\bar{\psi}d\psi \in \text{Im } \mathbb{H}$  and hence  $\tilde{p}\bar{\psi}i\psi\bar{\psi}id\psi = \tilde{p}\bar{\psi}d\psi \in \text{Im } \mathbb{H}$ . Also, since  $s \times \Delta s \in \text{Im } \mathbb{H}$  and orthogonal to  $s$ ,  $s(s \times \Delta s) \in \text{Im } \mathbb{H}$  and hence  $\text{Re}(s(s \times \Delta s)\mu) = -\frac{1}{2}\langle s \times (s \times \Delta s), ds \rangle = \frac{1}{2}\langle \Delta s, ds \rangle$ .

Differentiating the rhs of Eq. (14), multiplying on the left with  $-\bar{\psi}i$ , and taking the real part leaves only

$$\begin{aligned} -\frac{\hbar}{4}\text{Re}(\bar{\psi}d\psi(s \times \Delta s)) + d\tilde{p} &= -\frac{\hbar}{4}\text{Re}(s(\tilde{\eta} - \frac{1}{2}ds)(s \times \Delta s)) + d\tilde{p} \\ &= \frac{\hbar}{8}\langle s \times ds, s \times \Delta s \rangle + d\tilde{p}. \end{aligned}$$

It follows that the velocity 1-form  $\eta$  evolves as

$$\dot{\eta} + \mathcal{L}_v\eta = \hbar d\tilde{p} + \frac{\hbar^2}{4}\langle \Delta s, ds \rangle.$$

## D Discrete Circulation

Here we prove that the discrete velocity 1-form is given by

$$\eta_{vw} = \hbar \arg \langle \psi_v, \psi_w \rangle_{\mathbb{C}},$$

and arises, as is standard, from computing the circulation of the smooth velocity 1-form along the straight edge  $vw$

$$\eta_{vw} = \hbar \int_{vw} \langle d\psi, i\psi \rangle_{\mathbb{R}}.$$

This formula presupposes that we have chosen along  $vw$  a curve  $\gamma: [0, 1] \rightarrow \mathbb{C}^2$ ,  $|\gamma(t)|^2 = 1$  that interpolates between  $\psi_v$  and  $\psi_w$ . We will assume  $\langle \psi_v, \psi_w \rangle_{\mathbb{C}} \neq 0$ , so there is a unique shortest geodesic path  $c: [0, 1] \rightarrow \mathbb{S}^2$  with  $c(0) = \psi_v i \psi_v$  and  $c(1) = \psi_w i \psi_w$ . We will construct  $\gamma$  in such a way that  $\bar{\gamma}i\gamma = c$ .

We distinguish two cases: (1)  $\psi_v$  and  $\psi_w$  are linearly dependent or (2) independent, and construct  $\gamma$  explicitly in each case.

Suppose they are dependent, i.e.,  $\psi_w$  is a complex scalar multiple of  $\psi_v$ , then in fact  $\psi_w = e^{i\eta_{vw}}\psi_v$ . Letting  $\alpha: [0, 1] \rightarrow \mathbb{R}$  with  $\alpha(0) = 0$  and  $\alpha(1) = \eta_{vw}$ ,  $\gamma(t) := e^{i\alpha(t)}\psi_v$  will serve our purposes and

$$\hbar \int_0^1 \langle d\gamma, i\gamma \rangle_{\mathbb{R}} = \hbar \int_0^1 d\alpha = \eta_{vw} = \hbar \arg \langle \psi_v, \psi_w \rangle_{\mathbb{C}}, \quad (16)$$

since  $\langle d\gamma, i\gamma \rangle_{\mathbb{R}} = \langle i d\alpha \gamma, i\gamma \rangle_{\mathbb{R}} = d\alpha$ .

Suppose now that  $\psi_v$  and  $\psi_w$  are independent, i.e.,  $\langle \psi_v, \psi_w \rangle_{\mathbb{C}} = \cos(\beta)e^{i\eta_{vw}}$ , with  $\eta_{vw} \in (-\pi, \pi)$  and  $\beta \in (0, \pi/2)$ . Define  $\phi := \csc(\beta)(e^{-i\eta_{vw}}\psi_w - \cos(\beta)\psi_v)$ . One easily checks that  $\langle \psi_v, \phi \rangle_{\mathbb{C}} = 0$ ,  $|\phi|^2 = 1$  and

$$\psi_w = e^{i\eta_{vw}}(\cos(\beta)\psi_v + \sin(\beta)\phi)$$

Let now  $\gamma(t) := e^{i\alpha(t)}(\cos(\beta t)\psi_v + \sin(\beta t)\phi)$  and substitute in Eq. (16) to find the desired result.

## E Laplacian Eigenvalues

To use Fourier methods for Schrödinger integration as well as the Poisson solve we need the eigenvalues of the 3D Laplacian. Letting the index of a vertex be  $v = x, y, z$ , the spatial resolution becomes a triple of edge lengths  $l = (l_x, l_y, l_z)$ , and the overall cube measures  $L = (l_x N_x, l_y N_y, l_z N_z)$ .

The eigenvalues for the discrete ( $\tilde{\lambda}$ ) resp. continuous ( $\lambda$ ) Laplacian on a periodic domain are

$$\tilde{\lambda}_v = -\frac{4}{l_x^2} \sin^2\left(\frac{\pi x}{N_x}\right) - \frac{4}{l_y^2} \sin^2\left(\frac{\pi y}{N_y}\right) - \frac{4}{l_z^2} \sin^2\left(\frac{\pi z}{N_z}\right) \quad (17)$$

$$\lambda_v = -(2\pi)^2 \left( \frac{x^2}{l_x^2} + \frac{y^2}{l_y^2} + \frac{z^2}{l_z^2} \right). \quad (18)$$

The corresponding eigenvalues for the 3D Laplacian with Neumann boundary conditions, i.e., flow tangential to the wall, arise from Eqs. (17) and (18) by replacing  $L \leftarrow 2L$ . In that case the DCT replaces the FFT in Algs. 2 and 3.

In the continuous case Eq. (18) can be checked by direct differentiation of the Fourier basis, while Eq. (17) uses a centered second difference and some straightforward trigonometric identities.